ADVANCED FUNCTIONAL MATERIALS
www.afm-journal.de

Three Dimensional PtRh Alloy Porous Nanostructures: Tuning the Atomic Composition and Controlling the Morphology for the Application of Direct Methanol Fuel Cells

Yuan Zhang, Metini Janyasupab, Chen-Wei Liu, Xinxin Li, Jiaqiang Xu,* and Chung-Chiun Liu*

A strategy for the synthesis of PtRh alloy 3D porous nanostructures by controlled aggregation of nanoparticles in oleylamine is presented. The atomic ratio between the two components (Pt and Rh) is tuned by varying the concentration of precursor salts accommodating the oxidation of methanol. The morphology of PtRh alloy nanostructure is controlled by elevating the temperature of the reaction system to 240 °C. The prepared 3D porous nanostructures provide a high degree of electrochemical activity and good durability toward the methanol oxidation reaction compared to those of the commercial Pt/C (E-TEK) and PtRh nanoparticles. Therefore, the 3D alloy porous nanostructures provide a good opportunity to explore their catalytic properties for methanol oxidation.

1. Introduction

Platinum (Pt) is the most commonly used catalyst for the application of fuel cells. However, using a Pt catalyst in fuel cells can cause serious technological issues. Pt can be poisoned by CO and/or other contaminants during the oxidation of the fuel. Also, the durability of the electrode materials are critical, and Pt is not durable.[1,2] There has been considerable interest in developing more efficient and stable electrocatalysts to overcome these limitations. A frequently used strategy to design highly efficient catalysts in DMFCs is the use of multicomponent catalysts, such as random alloys, intermetallic alloys, near surface alloys, and core/shell particles.[3–6] The advantage of bimtallic or multi-metallic alloy materials is that their properties may be tuned by not only their size and geometries, but also by their composition.[4,7,8] The synergistic effect of multicomponent catalysts has been discussed by many researchers.[9–11] For instance, alloying iridium (Ir) with a secondary metal (Sn), both bifunctional effects and electronic modification between the two components in DEFC reaction can be optimized by controlling the different ratio of Sn and Ir atoms.[12]

The control of morphology for improving the properties of nanomaterials has been carried out in multiple applications, such as catalytic and sensor applications.[13,14] From the electronic structure aspect, small metal nanoparticles, particularly in the size range below ~5 nm, are defined in the "mitohedrical" region,[15,16] in which pronounced nanosize effects can be found. Its highly accessible surface area appears in a fundamentally difference from the bulk. Serious Ostwald ripening and associated crystallite growth (minimizing the total surface energy), usually occurred when the surface energy increased with decreasing particle size, further resulting in the loss of surface area in the electrocatalysts based fuel cell environments.[17,18] In order to avoid this phenomenon, organic capping agents are used to stabilize nanoparticles in relatively mild conditions. Unfortunately, these capping agents affect the catalyst surface resulting in reduced activity of the catalyst due to diffusion limitations and/or blocking of active sites.[19] Therefore, turning bimetallic nanoparticles into 3D porous materials may be preferred over separate nanoparticles due to their stability and comparable active surface area.[20–23] The 3D porous nanostructure is comprised of interconnected metallic particles or filaments, which provide a larger surface area and facilitates the effective transport of reactants and products. Therefore, the electrocatalytic performance of the catalysts can be improved. The 3D porous nanostructures have been studied extensively,[24,25] however, the investigation of 3D porous nanostructures constructed using alloy nanoparticles as building blocks has been rather limited.[21,26]

Y. Zhang, Prof. J. Xu
Department of Chemistry
Shanghai University
Shanghai 200444, China
E-mail: xujiaqiang@shu.edu.cn
Y. Zhang, M. Janyasupab, Prof. C.-C. Liu
Department of Chemical Engineering
Case Western Reserve University
Cleveland, OH 44106, USA
E-mail: yxz412@case.edu
C.-W. Liu
Institute of Material Sciences and Engineering
National Central University
Chung-Li 320, Taiwan
X. Li
State Key Laboratory of Transducer Technology
Shanghai Institute of Microsystem and Information Technology
Chinese Academy of Sciences
Shanghai 200050, China

DOI: 10.1002/adfm.201200678

Efforts have been directed toward the synthesis of 3D nanoporous bimetallic structures. However, the challenges in preparing these structures have been the control of alloying and porous structure. Most notably approach is through dealloying to prepare nanoporous metallic structures.[27,28] In order to form uniform porosity upon dealloying, the alloy system has to be in a monolithic phase because the porosity is formed by a self-assembly process through surface diffusion, rather than by the simple excavation of one phase from a pre-separated multiphase system.[29] Therefore, only limited crystalline alloy systems can form uniform nanoporous structures.[30]

In this research, a synthetic procedure to obtain 3D PtRh alloy porous nanostructures using oleylamine as both ligand and reducing agent is described. This method involves a simple one-step process in which "artificial atoms" (alloy nanoparticles) as uniform building blocks are used to construct the 3D alloy porous nanostructures. The ratio of the two components (Pt and Rh) is tuned to optimize the alloying effects and electronic modification in order to meet the needs of a high performance fuel cell. Consequently, the 3D porous PtRh nanostructures show enhanced catalytic activity and durability for the applications of DMFCs.

2. Results and Discussion

2.1. Characterization of PtRh Alloy 3D Porous Nanostructures

Figure 1 shows the morphology of prepared PtRh 3D porous nanostructures. The transmission electron microscopy (TEM) image at low magnification (Figure 1a) shows the morphology and size of the sample. The diameter of the aggregates is in the range of 50 to 90 nm. The mesostructure is further investigated by using highly magnified scanning electron microscopy (SEM) and TEM. Figure 1b reveals that each cluster is not a single crystal but is instead comprised of small particles. The high magnification SEM image (Figure 1c) elucidates the detailed morphology of 3D structures showing rough sphere-like aggregates where the small particles with the diameter of 2–3 nm were observed. The high-angle annular dark field (HAADF) image in Figure 1d illustrates the bicontinuous structure, consisting of an interconnected network of nanometer-sized PtRh crystallites and an interconnected pore space.

The 3D porous structures were obtained by subsequently increasing the temperature to 240 °C in the presence of oleylamine. First, initial PtRh nanoparticles were obtained by oleylamine acting as a reducing agent, and then the formed PtRh nanoparticles were covered with ligands with the assistance of oleylamine under the regulation of van der Waals interactions among alkyl chains. This was a complex process and sensitive to changes in the surrounding environment. The adjacent nanoparticles spontaneously aggregated into close-packed clusters at elevated temperature reducing the total energy of the whole particles system. This was due to a rapid decrease in surface ligand coverage caused by sudden decomposition of the precursor at high temperatures in a strong redox reaction.[31] The surface ligands could be decomposed at temperatures above 220 °C in the oleylamine/oleic acid solvent system.[32] Therefore, a high temperature resulted in the reduction of surface ligands and aggregated nanoparticles into 3D porous nanostructures. After the completion of the reaction, oleylamine was removed with hexane; therefore this process would not affect the electrochemical measurements.

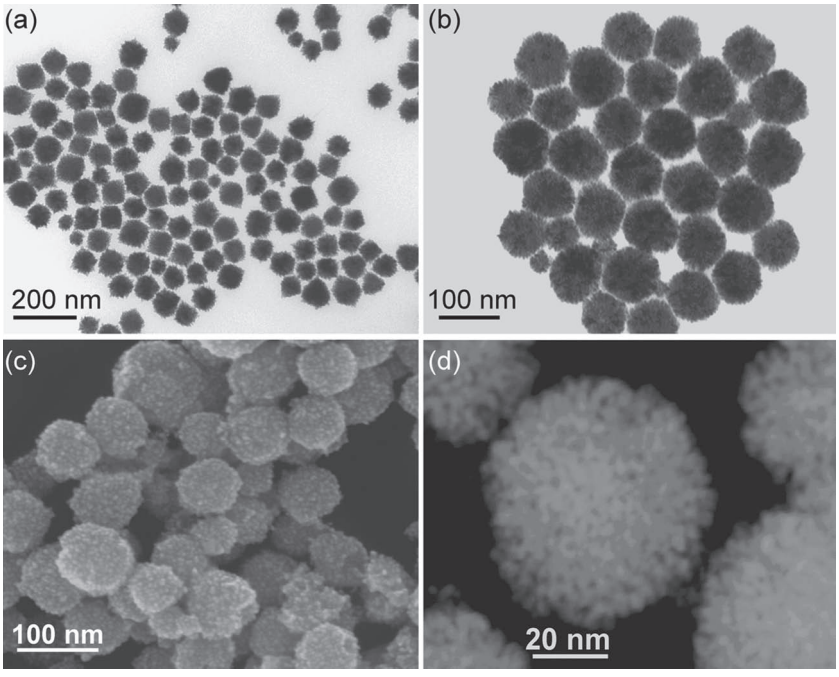

Figure 1. Morphology characterization of PtRh 3D porous nanostructures: a) low magnification TEM image; b) high magnification TEM image; c) high magnification SEM image; and d) HAADF image.

An annular dark-field scanning transmission electron microscopy (STEM) image, together with selected-area element analysis greyscale mapping of Pt and Rh (**Figure 2**), showed that both Pt (green) and Rh atoms (purple) were distributed through the whole area, revealing a homogeneous distribution of Pt and Rh in the 3D porous nanostructures. Based on the greyscale mapping images of the two elements, the signal intensity of Pt was much higher than that of Rh atoms. Furthermore, the line profiles (**Figure 3**) of the corresponding compositions on individual PtRh 3D porous nanostructures also revealed the elemental composition of the bimetallic materials, consisting of the higher Pt content in the sample, which was in excellent agreement with the elemental mapping results. Randomly selected small nanoparticles were used for the energy dispersive spectra (EDS) point analyses (see Supporting Information Figure S1), demonstrating the coexistence of Pt and Rh atoms distributed within the interior of same particles. The elemental compositions of different samples were obtained from EDS analysis (shown in **Table 1**). X-ray diffraction (XRD) analyses (Supporting

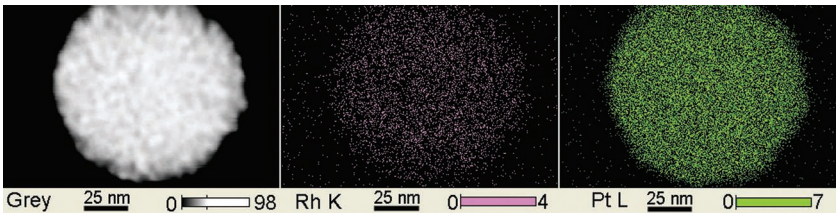

Figure 2. Pt and Rh EDX maps corresponding to the dark-field STEM image.

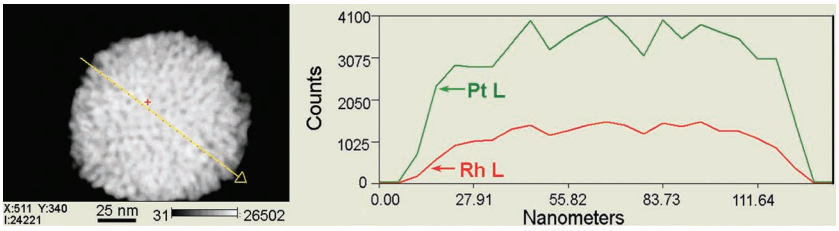

Figure 3. The cross-sectional compositional line profiles of an individual PtRh 3D nanostructure.

Information Figure S2) showed the characteristic peaks of PtRh 3D alloy nanostructures with different metal ratio. The higher angle shift of the peaks with increasing Rh content was observed, indicating the decreased d-spacings and contraction of the lattice constant. The XRD peaks shift to a larger angle was due to the incorporation of increasing Rh atoms into the Pt fcc lattice,[33] accounting for the alloy formation between Pt and Rh. These results indicated that PtRh 3D porous nanostructures were constructed from small PtRh alloy nanoparticles as the building blocks.

2.2. Methanol Oxidation Measurements

Methanol was an effective fuel for potential fuel cell application. Mechanistically, methanol was oxidized to CO_2 via a CO or $HCOO^-$ reactive intermediates.[34] Both of these pathways required a catalyst, which should be able to: a) dissociate the C-H bond and b) facilitate the reaction of the resulting residue with O-containing species forming CO_2 (or HCOOH). Otherwise, the formation of strongly adsorbed linearly bonded CO would result in the self-poisoning of Pt electrocatalysts.

Table 1. Relative compositions of Pt and Rh atoms obtained from EDS and XPS analysis.

Sample	Element	at% (results from EDS)	at% (results from XPS-before)	at% (results from XPS-after)
PtRh-1	Rh	11.47	46.70	–
	Pt	88.53	53.30	–
PtRh-2	Rh	15.58	55.50	55.20
	Pt	84.42	44.50	44.80
PtRh-3	Rh	19.84	59.55	55.79
	Pt	80.16	40.55	44.21

Platinum was recognized to be the best catalyst for breaking the C-H bond. However, there was a need to identify another metal (or metals) to activate water in order to provide the needed oxygen for the complete oxidation of methanol to CO_2. Therefore, PtRh 3D alloy porous nanostructures with different metal ratios were used to evaluate their performance in methanol oxidation.

The electrocatalytic activity of PtRh porous 3D nanostructures were analyzed in 0.5 M H_2SO_4 and 1 M CH_3OH solution using cyclic voltammetry. **Figure 4** shows the cyclic voltammograms for methanol oxidation over PtRh catalysts with different metal ratio in a solution of 0.5 M H_2SO_4 and 1 M CH_3OH. The potential was swept between -0.2 and 1.2 V versus saturated calomel electrode (SCE) at 50 mVs^{-1}. The ratio of peak currents associated with the anodic peaks in forward (I_f) and reverse (I_b) was used to describe the tolerance of a catalyst to intermediates generated during the oxidation of methanol.[27,35] A low I_f/I_b ratio indicated poor electrooxidation of methanol to carbon dioxide (CO) during the forward scan, suggesting excessive accumulation of carbonaceous intermediates on the catalyst surface.[10] For PtRh-3 catalyst, the value of I_f/I_b was 5.31, which was distinctly larger than that of PtRh-1 and PtRh-2. Commercial Pt catalyst (Pt E-TEK) with the same amount of Pt loading was also tested following the same protocol. The I_f/I_b value of Pt E-TEK (0.88) catalyst was significantly less than that of PtRh catalysts. Clearly, an increasing Rh content in the PtRh catalysts resulted in an improved poison tolerance as indicated from the I_f/I_b ratio.

The I_f/I_b value of PtRh-1 catalyst with a low Rh content was 1.05, which did not appear to process the improved CO poison tolerance than that of the Pt commercial catalyst (I_f/I_b = 0.88).

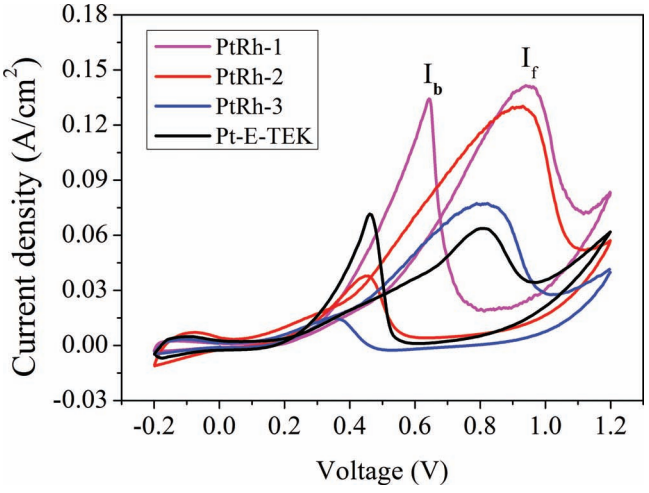

Figure 4. The cyclic voltammograms for methanol oxidation over PtRh samples with different atomic ratio (defined as PtRh-1, PtRh-2 and PtRh-3) in a solution of 0.5 M H_2SO_4 and 1 M CH_3OH.

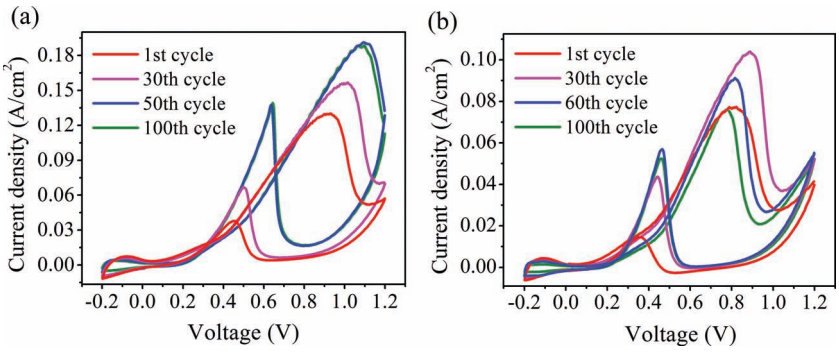

Figure 5. The cyclic voltammograms of the two PtRh samples in a solution of 1 M methanol and 0.5M H_2SO_4 at a potential scan rate of 50 mV s^{-1}: a) PtRh-2 and b) PtRh-3.

Therefore, only relatively high Rh content catalysts were further considered for the durability study of PtRh catalysts. The cyclic voltammograms of the two PtRh samples in a solution of 1 M methanol and 0.5M H_2SO_4 at a potential scan rate of 50 mV s^{-1} for 100 cycles are shown in **Figure 5**. For a moderate Rh content, the current density of the first scan at both forward and reverse peaks increased from 0.037 and 0.130 A/cm^2 to 0.075 and 0.150 A/cm^2 in the 30th cycle, and then continuously increased to 0.140 and 0.195 A/cm^2 in the 50th cycle, respectively. After 50 cycles the current density at both peaks retained in the same range (shown in Figure 5a). For PtRh-3 catalysts, an increase in current density at forward peak was observed in 30 cycles. After 30 cycles, the current density at the forward peak gradually decreased from 0.103 A/cm^2 in the 30th cycle to 0.090 A/cm^2 in the 60th cycle, in contrasting to the current density which continuously increased at the reverse peak (shown in Figure 5b). Furthermore, the current density decreased at both forward and reverse peak after 60 cycles. The decrease of current density with cycling could be due to the dissolution of Rh in the electrolyte during the electrocatalysis.[36,37] Comparing the I_f/I_b ratio of the two catalysts, the tolerance factors of PtRh-3 were 1.45 after 100 cycles, which was similar to that of PtRh-2 (1.44) and significantly lower than the original value (I_f/I_b = 5.31) after running 100 cycles. It was clear that the higher Rh content did not provide a better poison tolerance.

2.3. XPS Analysis

X-ray photoelectron spectroscopy (XPS) measurements were used to determine the surface composition changes before and after 100 cycles in the electrochemical environment. The relative compositions of Pt and Rh on the surface of PtRh catalysts were obtained by analyzing XPS data (Table 1). The relative higher Rh content was observed in the three XPS analysis results, suggesting that the clean surface was strongly Rh-enriched, which was observed in all samples.

The stabilization effect of Rh on PtRh porous 3D nanostructures became apparent based on the XPS analysis of the samples with relatively higher Rh content after 100 cycles. The XPS analysis showed a mild loss of Rh content in PtRh-3 catalyst (shown in Table 1, results from XPS). After 100 cycles, the PtRh-2 catalyst contained Pt and Rh with an atomic ratio at 55:44, which was almost the same as the original ratio. However, Rh content in the PtRh-3 samples showed a mild decrease. These observations indicated that the excess Rh atoms in the PtRh-3 alloy sample were unalloyed Rh atoms, dissolving during methanol oxidation, and further decreased the capacity of poison tolerance. We also measured the cyclic voltammograms of PtRh-2 and PtRh-3 catalysts in 0.5 M H_2SO_4 electrolyte after synthesis and developed during the cycling process (shown in Supporting Information Figure S3). After comparing the cyclic voltammograms of PtRh-2 and PtRh-3 catalysts, we found that the cyclic voltammograms of PtRh-2 catalyst remained unchanged over cycling in the electrochemical environment. While the peaks in the hydrogen adsorption-desorption region of PtRh-3 catalyst showed a slightly increase, which could be associated with the increasing surface area of Pt by the dissolution of excess unalloyed of Rh species during the cycling treatment. This result is consistent with XPS analysis. Therefore, the content of Rh in alloy catalysts directly affected the methanol oxidation. According to these results, we suggested that the relatively poor poison tolerance of a higher Rh content may be attributed to the corrosion of Rh itself.

The relative compositions of Rh oxide in both PtRh-2 and PtRh-3 catalysts during the cycling process were increased in the XPS analysis, while the relative composition of Pt and Pt oxide remained (shown in Supporting Information Table S1). The Rh 3d spectra and Pt 4f spectra of the PtRh-2 and PtRh-3 catalysts were shown in Supporting Information Figure S4 and S5. In a theoretical study of CO oxidation on metals and metal oxides, Hu et al. reported that the reaction barrier was lower in the oxide than in the metal because of a change in the adsorption geometry of oxygen atoms.[38] Hence, the formation of Rh oxide on the surface of PtRh catalysts provided the higher catalytic activity for the CO oxidation, facilitating the electrocatalytic reaction of methanol.[39] Therefore, the increased current density in the first 50 cycles of the cyclic votammagrams could be attributed to the increased Rh oxide content on the surface of PtRh catalysts.

The methanol oxidation performance of Pt E-TEK commercial catalyst and PtRh alloy nanoparticles (~5 nm) with controlled Rh content were investigated. The current density of PtRh-2 3D nanostructures was nearly twice as high as that of Pt E-TEK catalyst and PtRh nanoparticles. The enhanced catalytic activity could be attributed to the more active adsorption sites of the larger surface area and the interconnected particles accelerating the transport rate of the reactive species. After 1300 cycles as shown in **Figure 6**, the PtRh nanoparticles lost about 80% of their current density, indicating the poor durability of this electrocatalyst. Pt E-TEK catalysts also showed a distinct decrease in current density. For comparison, the current density of prepared PtRh-2 3D catalyst almost remained a stable value.

The growth of the particles and the corrosion of PtRh nanoparticles during electrocatalytic detection (shown in **Figure 7**a,b) were observed, while PtRh 3D alloy nanostructures survived after 1300 cycles (Figure 7c). For the same ratio

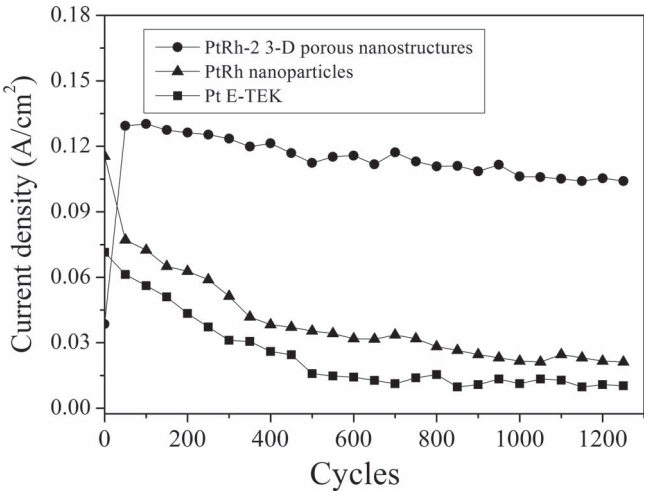

Figure 6. The durability performance of PtRh-2 3D porous nanostructures, PtRh nanoparticles, and Pt E-TEK catalysts.

of PtRh catalysts, however, with different morphology and size, the stability of the materials could be different. Nanoparticles with the diameter of 5 nm during atomic migration via diffusion showed entire crystallites along the surface with time in an electrochemical environment. Therefore, the growth of large crystallites at the expense of small ones (so-called Ostwald ripening) could be observed. Consequently, the PtRh catalysts with 3D porous structures enhanced the current density and durability toward methanol oxidation compared to those of PtRh nanoparticles. Therefore, by alloying a second metal with controlled atomic composition and tuning the alloy particles into 3D porous structures, the catalyst properties can be tailored to accommodate the application of DMFCs.

3. Conclusions

The PtRh alloy 3D porous nanostructure catalyst was designed, and used for methanol oxidation. The PtRh alloy 3D porous nanostructures were synthesized by a modified template-free self-assembly approach. In the synthesis, oleylamine was initially used as a reducing agent to obtain PtRh nanoparticles and then as the ligand to aggregate particles to 3D porous nanostructures. The PtRh catalysts with a moderate Rh content (~15 wt%) showed good poison tolerance for the oxidation of methanol. The dissolution of Rh atoms was observed for PtRh catalysts with excess Rh content, suggesting the unalloyed Rh atoms would result in a self-adjusted dissolution capability of PtRh catalysts. Furthermore, the formation of Rh oxide in the initial 50 cycles enhanced the electrocatalytic activity toward methanol oxidation. The 3D porous nanostructures continuously accelerated reactant transfer, improving the catalytic activity of PtRh alloy. Therefore, the PtRh alloy 3D porous nanostructures with controlled atomic composition and morphology showed higher catalytic and better durability performance for methanol oxidation compared with PtRh nanoparticles and commercial Pt E-TEK catalysts. This concept of alloying a second metal with controlled atomic composition and tuning the alloy particles into 3D porous structures represents a new and meaningful approach towards designing high-performance, multifunctional nanostructured catalysts for the future fuel cells applications.

4. Experimental Section

Synthesis: The PtRh 3D alloy porous nanostructures were prepared by a modified template-free self-assembly approach.[40] Typically, 10 mL of oleylamine was added to a 25 mL three-neck flask in air, and heated up to 120 °C, maintaining at this temperature for 10 min. Then 0.055 g of $H_2PtCl_6{\cdot}6H_2O$ and 0.012 g of $RhCl_3$ were added. After the reactants dissolved, the mixture was heated to 220 °C, and this reaction proceeded for 10 min at this temperature. The mixture was then continuously heated up to 240 °C, and stirred for another 10 min. Black precipitate was then collected by centrifugation at 16,000 rpm (Sorvall RC-5C Centrifuge) for 20 min. The slurry was washed with hexane several times and placed into a vacuum oven at 60 °C for 8 h or more. Then, the final PtRh sample with Rh content of ~15 wt% was obtained.

Three different ratios of PtRh catalysts (PtRh-1, PtRh-2 and PtRh-3) were prepared. The Rh content in three samples was about 10 wt%, 15 wt% and 20 wt%, respectively. The other PtRh catalysts with different Rh content were obtained by adjusting the concentrations starting from the precursors using the same procedure. For the comparison with 3D PtRh catalyst, PtRh alloy nanoparticles (~5 nm) with controlled same Rh content were synthesized through ethylene glycol reduction with the assistance of rapid microwave irradiation. In the synthesis of PtRh nanoparticles, the starting mixture contained 25 ml ethylene glycol (EG), 0.018 g of $K_2PtCl_6{\cdot}6H_2O$, 0.002 g of $RhCl_3$ and 0.75 mL of 0.4 M KOH in a 300 mL beaker. The beaker was placed in the center of a household microwave oven (Panasonic, 1250 W) and heated for 30 s, the PtRh nanoparticles with the diameter of ~5 nm were obtained.

Characterization: X-ray diffraction (XRD) patterns were obtained on a powder X-ray diffractometer (Scintag X-1, USA) operating at 40 kV and 40 mA and using Cu Kα radiation (λ = 1.54056 Å). The XRD data were collected at a scanning rate of 0.02 ° s^{-1} for 2θ in a range from 30 °C to 90 °C.

Transmission electron microscopy (TEM) was performed with a JEM-200CX operated at 160 kV. Element analysis mapping and energy dispersive spectra (EDS) line scanning were obtained by scanning transmission electron microscopy (STEM) combined with energy dispersive X-ray spectrometry (EDXS). The STEM image, EDX elemental maps and line profiles were determined by a LIBRA 200FE microscope (Zeiss Instrument, 200 kV) equipped with an aberration-corrected in-column OMEGA energy filter with the advantages of a field-emission gun and Köhler illumination. Scanning electron microscopy (SEM) was carried out by Helios NanoLab 650 (FEI, 10 kV) featured with integrated monochromator (UC) and beam deceleration delivering sub-nanometer resolution on 3D nanostructure characterization.

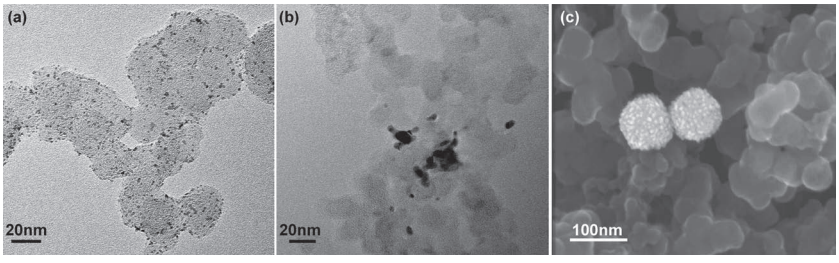

Figure 7. TEM and SEM images of PtRh catalysts on carbon support: a) PtRh nanoparticles before 1300 cycles running, b) PtRh nanoparticles after 1300 cycles running, and c) PtRh 3D nanostructuers after 1300 cycles running.

X-ray photoelectron spectroscopy (XPS) was carried out using a PHI 680 system with a monochromatic Al Ka source (1,486.6 eV). For XPS analysis, the catalyst solution was placed onto a silicon wafer and put into an ultrahigh vacuum (UHV) chamber ($\leq 9.9 \times 10^{-9}$ torr) housing the analyzer. The binding energies were calculated with respect to C (1s) at 284.6 eV and were measured with a precision of 0.2 eV.

Methanol Oxidation Measurements: The prepared catalysts powder (0.02 g) was re-dispersed in ethanol (10 mL) to prepare 2 mg/mL of a PtRh catalyst solution. The resulting PtRh catalyst solution (3.2 mL) was mixed with 16 mg of carbon powder (Vulcan XC 72R, Cabot, USA) by ultrasound for 2 h and used for electrochemical characterization, respectively. For the preparation of electrocatalyst, 8.0 mg of metal/carbon powder was suspended in a 200 µL of ethanol and 100 µL of Nafion solution (5 wt%), and then ultrasonically blended for 30 min. forming the thick film printing ink, and 4 µL of the catalyst ink which was placed onto the surface of a glassy carbon disk electrode (geometric area of 0.196 cm^2). The catalyst-coated electrode was then dried under ambient condition for 3 min. The loading of total metals was controlled to 150 $\mu g/cm^2$. The current density was expressed by the geometric area of the electrode.

The five-neck cell chamber featured one center neck which was used to accommodate a rotating working electrode (900 r. p. m.), two side necks to mount reference and platinum wire counter electrodes and two gas inlet/outlets. The electrolyte was a N_2-saturated 0.5 M H_2SO_4 solution. In the CV measurements, the electrode potential was scanned in the range of –0.2 to 1.2 V versus saturated calomel electrode (SCE). The catalyst electrodes were cleaned before data collection with a steady-state CV scanned for 50 cycles in the range of –0.2 to 1.2 V versus SCE at 0.1 V/s. All electrochemical experiments were carried out at room temperature and ambient pressure.

Supporting Information

Supporting Information is available from the Wiley Online Library or from the author.

Acknowledgements

This work was supported by DOD Air Force Office of Research MURI-2011-Nanofabraication and NSFC (61071040) Grant. China Scholarship Council Postgraduate Scholarship Program, Royal Thai Government Scholar Fellowship, Taiwan National Central University Fellowship, Delta Environmental and Education Foundation, and Leading Academic Discipline Project of Shanghai Municipal Education Committee (J50102) are gratefully acknowledged.

Received: March 12, 2012
Published online: May 18, 2012

[1] V. Mazumder, Y. Lee, S. H. Sun, *Adv. Funct. Mater.* **2010**, *20*, 1224.
[2] H. S. Liu, C. J. Song, L. Zhang, J. J. Zhang, H. J. Wang, D. P. Wilkinson, *J. Power Sources* **2006**, *155*, 95.
[3] Z. H. Zhang, Y. Wang, X. G. Wang, *Nanoscale* **2011**, *3*, 1663.
[4] Y. Liu, M. F. Chi, V. Mazumder, K. L. More, S. Soled, J. D. Henao, S. H. Sun, *Chem. Mater.* **2011**, *23*, 4199.
[5] S. Zhou, G. S. Jackson, B. Eichhorn, *Adv. Funct. Mater.* **2007**, *17*, 3099.
[6] F. Taufany, C. J. Pan, J. Rick, H. L. Chou, M. C. Tsai, B. J. Hwang, D. G. Liu, J. F. Lee, M. T. Tang, Y. C. Lee, C. I. Chen, *ACS Nano* **2011**, *5*, 9370.
[7] V. R. Stamenkovic, B. S. Mun, K. J. J. Mayrhofer, P. N. Ross, N. M. Markovic, *J. Am. Chem. Soc.* **2006**, *128*, 8813.
[8] C. Wang, M. Chi, G. Wang, D. Vliet, D. Li, K. More, H. H. Wang, J. A. Schlueter, N. M. Markovic, V. R. Stamenkovic, *Adv. Funct. Mater.* **2011**, *21*, 147.
[9] Z. M. Peng, H. J. You, H. Yang, *Adv. Funct. Mater.* **2010**, *20*, 3734.
[10] Y. H. Lee, G. Lee, J. H. Shim, S. Hwang, J. Kwak, K. Lee, H. Song, J. T. Park, *Chem. Mater.* **2006**, *18*, 4209.
[11] E. Casado-Rivera, D. J. Volpe, L. Alden, C. Lind, C. Downie, T. Vazquez-Alvarez, A. C. D. Angelo, F. J. DiSalvo, H. D. Abruna, *J. Am. Chem. Soc.* **2004**, *126*, 4043.
[12] W. X. Du, Q. Wang, D. Saxner, N. A. Deskins, D. Su, J. E. Krzanowski, A. I. Frenkel, X. W. Teng, *J. Am. Chem. Soc.* **2011**, *133*, 15172.
[13] L. Y. Chen, T. Fujita, Y. Ding, M. W. Chen, *Adv. Funct. Mater.* **2010**, *20*, 2279.
[14] L. F. Liu, Z. P. Huang, D. A. Wang, R. Scholz, E. Pippel, *Nanotechnology* **2011**, *22*, 105604.
[15] G. C. Bond, *Chem. Soc. Rev.* **1991**, *20*, 441.
[16] A. Cao, G. Veser, *Nat. Mater.* **2010**, *9*, 75.
[17] E. Guilminot, A. Corcella, F. Charlot, F. Maillard, M. Chatenet, *J. Electrochem. Soc.* **2007**, *154*, B96.
[18] E. Guilminot, A. Corcella, M. Chatenet, F. Maillard, F. Charlot, G. Berthome, C. Iojoiu, J. Y. Sanchez, E. Rossinot, E. Claude, *J. Electrochem. Soc.* **2007**, *154*, B1106.
[19] A. Cao, R. Lu, G. Veser, *Phys. Chem. Chem. Phys.* **2010**, *12*, 13499.
[20] Q. B. Zhang, J. P. Xie, J. Liang, J. Y. Lee, *Adv. Funct. Mater.* **2009**, *19*, 1387.
[21] J. I. Shui, C. Chen, J. C. M. Li, *Adv. Funct. Mater.* **2011**, *21*, 3357.
[22] E. A. Anumol, A. Halder, C. Nethravathi, B. N. Viswanath, Ravishankar, *J. Mater. Chem.* **2011**, *21*, 8721.
[23] C. H. Cui, H. H. Li, S. H. Yu, *Chem. Sci.* **2011**, *2*, 1611.
[24] Y. X. Zhang, H. C. Zeng, *J. Phys. Chem. C* **2007**, *111*, 6970.
[25] Y. Ding, M. W. Chen, J. Erlebacher, *J. Am. Chem. Soc.* **2004**, *126*, 6876.
[26] B. C. Tappan, S. A. Steiner, E. P. Luther, *Angew. Chem. Int. Ed.* **2010**, *49*, 4544.
[27] L. Chen, H. Guo, T. Fujita, A. Hirata, W. Zhang, A. Inoue, M. Chen, *Adv. Funct. Mater.* **2011**, *21*, 4364.
[28] B. C. Tappan, S. A. Steiner, E. P. Luther, *Angew. Chem. Int. Ed.* **2010**, *49*, 4544.
[29] J. Erlebacher, M. J. Aziz, A. Karma, N. Dimitrov, K. Sieradzki, *Nature* **2001**, *410*, 450.
[30] J. S. Yu, Y. Ding, C. X. Xu, A. Inoue, T. Sakurai, M. W. Chen, *Chem. Mater.* **2008**, *20*, 4548.
[31] G. Q. Ren, Y. C. Xing, *Nanotechnology* **2009**, *20*, 465604.
[32] H. P. Zhou, Y. W. Zhang, H. X. Mai, X. Sun, Q. Liu, W. G. Song, C. H. Yan, *Chem. Eur. J.* **2008**, *14*, 3380.
[33] D. S. Wang, Q. Peng, Y. D. Li, *Nano Res.* **2010**, *3*, 574.
[34] A. Hamnett, *Catal. Today* **1997**, *38*, 445.
[35] S. C. Yang, Z. M. Peng, H. Yang, *Adv. Funct. Mater.* **2008**, *18*, 2745.
[36] M. Łukaszewski, H. Siwek, A. Czerwi´nski, *Electrochim. Acta* **2007**, *52*, 4560.
[37] M. Łukaszewski, A. Czerwin´ski, *J. Alloy. Compd.* **2009**, *473*, 220.
[38] X. Q. Gong, Z. P. Liu, R. Raval, P. Hu, *J. Am. Chem. Soc.* **2004**, *126*, 8.
[39] M. E. Grass, Y. W. Zhang, D. R. Butcher, J. Y. Park, Y. M. Li, H. Bluhm, K. M. Bratlie, T. F. Zhang, G. A. Somorjai, *Angew. Chem. Int. Ed.* **2008**, *47*, 8893.
[40] D. S. Wang, T. Xie, Q. Peng, Y. D. Li, *J. Am. Chem. Soc.* **2008**, *130*, 4016.